Monthly Notices of the ROYAL ASTRONOMICAL SOCIETY

MNRAS **501,** 3030–3045 (2021) doi:10.1093/mnras/staa3823
Advance Access publication 2020 December 11

FASS: a turbulence profiler based on a fast, low-noise camera

A. Guesalaga,[1]★ B. Ayancán,[1] M. Sarazin,[2] R. W. Wilson,[3] S. Perera[3] and M. Le Louarn[2]

[1]*Department of Electrical Engineering and Astro-Engineering Centre, Pontificia Universidad Católica de Chile, 4860 Vicuna Mackenna, Santiago 7820436, Chile*
[2]*European Southern Observatory, Karl-Schwarzschild-Strasse 2, D-8046 Garching bei Muenchen, Germany*
[3]*Department of Physics, Centre for Advanced Instrumentation, University of Durham, South Road, Durham DH1 3LE, UK*

Accepted 2020 December 8. Received 2020 December 8; in original form 2020 September 2

ABSTRACT

The measurement of the atmospheric optical turbulence with a new scintillation profiler is described and demonstrated. The instrument, FASS (Full Aperture Scintillation Sensor), uses new fast and low-noise detectors to record and process sequences of scintillation images. Statistical processing of these data is based on the calculation of power spectra of intensity in annular pupil zones over the angular coordinate. The angular power spectra are used to measure the optical turbulence intensity of 14 layers located at logarithmically spaced distances from 0.3 to 25 km. The reference functions relating turbulence strength to the angular power spectra are computed by numerical simulation. Measurement of the ground-later turbulence and total seeing with FASS is possible when the detector is conjugated to a negative (below ground) distance. Results of measurement campaigns at Paranal are reported, documenting a good agreement of turbulence profiles measured by FASS with two other instruments, SCIDAR and MASS.

Key words: atmospheric effects – adaptive optics – site testing.

1 INTRODUCTION

The characterization of atmospheric seeing and optical turbulence is a must in the design and operation of modern ground-based optical telescopes. Facility turbulence monitors play an important role for astronomical observations, optimization, performance prediction, and queue scheduling. Turbulence profiles are an essential element for selecting new observation sites. Seeing is generally measured using differential motion of star images from two slightly separated small apertures, and the Differential Image Motion Monitor (DIMM) site monitor has become a de facto standard (Sarazin & Roddier 1990; Tokovinin 2002). Modern observation techniques, such as adaptive optics (AO) and interferometry, require not only measurements of a global seeing, but also the information on the vertical turbulence distribution. This vertical profile is essential to evaluate the performance of adaptive optics systems, especially those with a wide field of view. Furthermore, it is well known (Kenyon et al. 2006) that the ultimate accuracy of photometry and astrometry depend on the vertical profile of optical turbulence.

In response to a constant demand for better characterization of the atmospheric turbulence, new techniques such as SCIDAR (Vernin & Roddier 1973), Stereo-SCIDAR (Shepherd et al. 2014; Osborn et al. 2018), Multi Aperture Scintillation Sensor (MASS; Kornilov et al. 2003), SLODAR (Wilson, Butterley & Sarazin 2009), and PML (Ziad et al. 2013) have been developed, providing useful results and improving our knowledge about these optical disturbances. MASS measures the atmosphere in six layers by analysing the spatial intensity fluctuations of the scintillation at the ground (Kornilov et al. 2003). The technique relies on the dependence of the spatial scale of scintillation (of the order of the Fresnel radius) on the propagation distance. Since MASS does not provide an estimation of turbulence below 0.5 km, the instrument is combined with a DIMM monitor to infer the missing ground layer, and deliver a full turbulence profile (Kornilov et al. 2007).

Whilst MASS has been a successful instrument, operating in many observatories around the world, there are two significant limitations. First, its vertical resolution is limited by coarse spatial sampling. Secondly, highly customized components of the MASS opto-mechanics and photon-counting electronics make its long-term maintenance problematic, as the original photomultipliers used as detectors are no longer available in the market. Fabrication of new MASS instruments would be therefore costly and impractical. The mature technology of electron-multiplying CCD detectors (EMCCD) together with a new family of low-noise solid-state detectors, referred as scientific CMOS (sCMOS), offer new alternatives to MASS, with potential lower costs and simplified designs. In the case of new sCMOS detectors, they offer quantum efficiencies (QE) higher than 80 per cent, readout noise around 1 $\bar{e}\,\mathrm{pixel}^{-1}$ and increasingly low costs. These features make them a suitable choice for low-light applications such as pupil imaging of beacon stars of magnitudes as faint as $m = 2.5$. Appendix A describes a methodology to determine the stars that can be used as beacons for this type of detectors.

2 THE FASS CONCEPT

The Full Aperture Seeing Sensor (FASS) is aimed to be a successor of MASS–DIMM, exploiting modern commercial-off-the-shelf sCMOS detectors to image the full aperture of the telescope in order to measure the atmospheric turbulence profile. It offers a substantial

★ E-mail: aguesala@ing.puc.cl

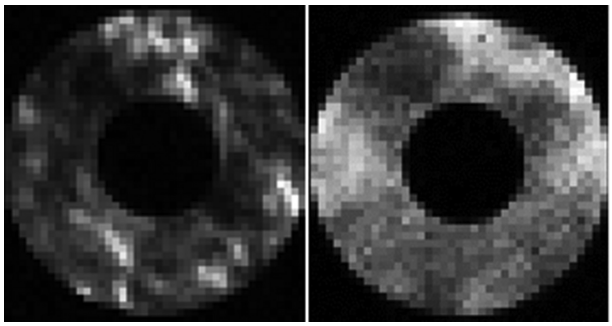

Figure 1. Scintillation patterns at the telescope pupil. Left: low altitude turbulence; right: high altitude turbulence (Celestron 9.5 arcsec telescope, 2018 April, Paranal).

improvement over the classic MASS–DIMM in terms of resolution, logistics, and cost. Its version with negative conjugation, currently under development, provides a full profile that includes the ground layer. In the FASS technique, the incoming light captured by a small size telescope (9.5 arcsec or 12 arcsec) is transferred to the detector, generating an image of scintillation patterns (speckles). All photon flux entering the aperture is used to form the image of the pupil, hence the name FASS.

We know from the theory of optical propagation through turbulence (Roddier 1981), that scintillation patterns caused by lower layers, will contain small speckles (Fig. 1, left-hand panel), whereas larger speckles will be formed by higher turbulent layers (Fig. 1, right-hand panel). This phenomena can be explained by the Fresnel formula $d_s \approx \sqrt{h\lambda}$, where d_s is the expected speckle diameter, h is the altitude of the corresponding layer, and λ is the wavelength considering a monochromatic source. For example, for $\lambda = 500$ nm, the average size of a speckle at 0.5 and 20 km are 1.6 and 10 cm, respectively. Hence, the scale of these spatial fluctuations (or better, their spectra), will tell us the altitude where the scintillation was originated.

2.1 Atmospheric parameters

Nowadays, the physics of light propagation through atmospheric turbulence is well understood and a comprehensive theory exists (Tatarskii 1961; Roddier 1981). A well accepted parameter to describe this turbulence is the refractive index structure constant, C_n^2, and the turbulence profile, $C_n^2(h)$ is defined as a function of altitude above an observation point $h = z\cos\gamma$, where z is the propagation distance along the line of sight and γ is the zenith angle. The quality of an image propagated through a turbulent path, called seeing, depends on $C_n^2(h)$. Instead of considering $C_n^2(h)$ as a continuous function of h, we take it as a collection of independent turbulent layers at altitude h_i. The intensity of those layers J_i are the integrals of $C_n^2(h)$ over the layers

$$J_i = \int_{i_{\rm th}\ \rm layer} C_n^2(z)\mathrm{d}z, \tag{1}$$

measured in $\mathrm{m}^{1/3}$. Then, the turbulence profile is completely defined by a set of h_i and J_i values, as it is the seeing parameter. Seeing is generally expressed in terms of the full-width at half-maximum of a point source image $\varepsilon_0 = 0.98\lambda/r_0$, where r_0 is the so-called Fried parameter, $r_0 = (0.423(2\pi/\lambda)^2 J)^{3/5}$. Since r_0 depends on the light wavelength, it is generally expressed for $\lambda = 500$ nm to avoid ambiguities. These definitions assume that optical turbulence is a stationary random process with a Kolmogorov spectrum.

2.2 Profile restoration

Following the procedure and notation in Tokovinin et al. (2003), we start defining the spectral weighting functions (SWF) for each layer which are stacked as rows in a matrix **W**. The SWFs describe some measurable statistical parameter of a scintillation signal produced by a single weak turbulent layer of unit strength located at a distance h_i. Here, we rely on the weak-amplitude approximation by assuming that the effect of multiple layers is a linear combination of effects produced by individual layers. In the case of FASS, the measurable parameter is the power spectral density (PSD) of intensity fluctuations in annular zones at the telescope pupil. There are as many SWFs as discrete layers i ($i = 1, .., N_h$), each of them corresponding to the PSD of the scintillation received at the detector, generated by each layer i acting individually. To obtain the complete set of SWFs, we use simulations. Kolmogorov phase screens with a known turbulence strength (characterized by the r_0 parameter) are generated and light propagation over distance h_i defines the scintillation at the detector. The PSD corresponding to each row in matrix **W** is computed. Then, assuming weak-scintillation conditions, we can express the scintillation PSD of a turbulence, $\hat{\boldsymbol{F}}$, as a linear function of **W**, i.e.

$$\hat{\boldsymbol{F}} = \boldsymbol{x}^T \mathbf{W} \tag{2}$$

where vector $\hat{\boldsymbol{F}}$ contains M frequency elements, **W** is a $N_h \times M$ matrix, and x is a column vector with N_h coefficients representing the turbulence integrals in each layer (superscript T indicates transpose). Next, we compute $\bar{\boldsymbol{F}}$, the average of many PSDs from the on-sky images captured by the detector. This vector is used to find the best match between the model $\hat{\boldsymbol{F}}$ and the data $\bar{\boldsymbol{F}}$ by searching the vector $\boldsymbol{x}$ of unknowns that minimizes the following merit function:

$$\chi^2 = \sum_{m=1}^{M} (\bar{\boldsymbol{F}} - \hat{\boldsymbol{F}})^2. \tag{3}$$

This search for the minimum is carried out using a least-squares method that can handle the non-negativity constraints imposed by the elements in vector $\boldsymbol{x}$. This is later described in Section 3.6.

3 THE FREE-ATMOSPHERE CASE

As noted earlier, scintillation-based profilers are blind to ground turbulence. However, it is still possible to apply the restoration method described above to zero altitude values of h by allowing the wavefront to propagate below the pupil. This 'defocusing' of the pupil, requires important changes in the optics, but very little in terms of the image processing and in the algorithms minimizing χ^2. Hence, we have two possible modes of operation:

(i) Free-atmosphere or pupil conjugation (PC herein): for turbulence layers typically above 500 or 1000 m, the telescope pupil is imaged, so near-the-ground turbulence is invisible due to poor scintillation the lack contrast and also because the smallest speckle size becomes comparable to the pixel size, making the profile restoration extremely sensitive to detector's noise and possibly, undersampled.

(ii) Negative conjugation (NC herein): in this mode (sometimes also referred to as the *generalized case*), the wavefront entering the telescope pupil is allowed to propagate below the aperture by means of additional optics. This extended propagation builds up scintillation speckles caused by all layers, including those close to the pupil which appears in the defocused images with sufficient contrast as to be detected.

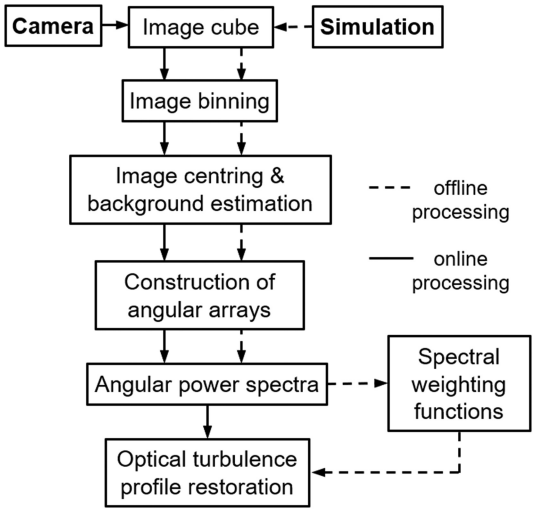

Figure 2. Data flow and processing.

Next, we describe the function blocks for the PC case and in Section 5 we will explain the modifications required to operate in the NC mode. The block diagram in Fig. 2 summarizes the data flow and the main functions that comprise the method. The two sources of data correspond to the camera images (continuous lines) and the simulated wavefronts propagated through the pre-defined layers (dashed lines) yielding the SWFs. The measured data are processed on-line and the simulated data are generated off-line and stored for the later profile restoration. A large stack of consecutive images (data cube), sampled at frame rates higher than 80 Hz yield $\bar{\boldsymbol{F}}$ and using the set of reference functions $\hat{\boldsymbol{F}}$ previously stored, the profile is obtained by minimizing equation (3).

3.1 Image centring and background estimation

A key pre-processing step performed on the images is the correction for background and the centring of the propagated pupil on the detector. Estimation of the background offset due to electronic biases is required for the spectrum calculation. As we will see in the following sections for the NC case, image motion can be particularly detrimental for the profile restoration so an instantaneous centring of the pupil image in the detector is essential and must be performed faster than the dynamics of the misalignment produced by tracking errors or external disturbances such as wind shaking or vibrations. An advantage of the NC mode is that deviations from the centre appear in the detector as a displacement of the propagated pupil, so additional imaging optics for star tracking is not necessary.

Fig. 3 shows an example of an off-centred pupil as seen by the detector and Fig. 4 shows the corresponding pixel histogram in number of photoelectrons generated (counts). As the plot shows, the resulting pattern normally starts with a high number of counts produced by a combination of the brightest scintillation speckles, noise, and hot pixels that rapidly decay down to a background level.

For bad seeing conditions, saturation in the scintillation pattern is possible, which could make the darker image zones indistinguishable from the background. We avoid this potential problem by: (i) averaging several consecutive images (e.g. 4), which at sampling rates above 80 Hz, still captures the edges of the pupil without significant blurring; and (ii) estimating the centre from the sum of row and column elements (see Fig. 5 for the horizontal case). It is interesting to note that in the NC case, detection of the pupil edges is

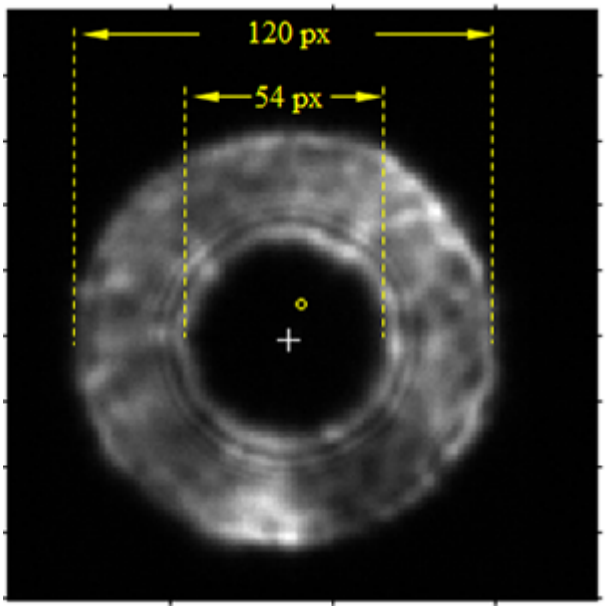

Figure 3. Average of four images of the propagated pupil to −400 m. The small circle is the centre of the active part of the detector and the cross corresponds to the centre estimated for the propagated pupil (camera: ASI290MM; star: Canopus, Santa Martina, 2020 March).

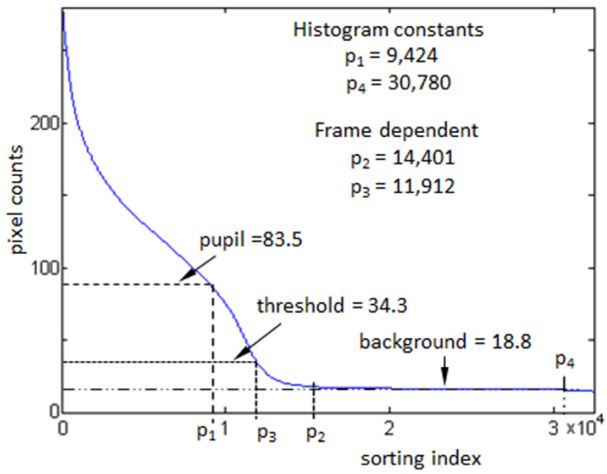

Figure 4. Histogram of pixel counts in descending order for the propagated pupil image. The dashed line (p_1) corresponds to the theoretical number of pixels inside the pupil mask (assuming no diffraction and accounting for the central obscuration. The x-coordinate point p_2 separate the pixels with no significant signal content and p_3 define the threshold over which a pixel is part of the propagated pupil that is used for the centre estimation. The dot–dashed line is the estimate of the image background calculated as the histogram average between p_2 and p_4.

helped by the outer (and strongest) diffraction ring, which in practice lifts the edges, mitigating possible fading under strong scintillation.

Our approach estimates the pupil centre and the image background simultaneously. First, the intensity threshold over which the image pixels can be considered part of the propagated pupil is estimated. An initial approximation for this threshold is to calculate the number of pixels that form the theoretical aperture without diffraction smearing. For this example, the radius of the inner and outer edges are 54 and 120 pixels, respectively (see Fig. 3), corresponding to 9424 pixels inside the pupil (p_1 in Fig. 4). In the NC mode, this number of

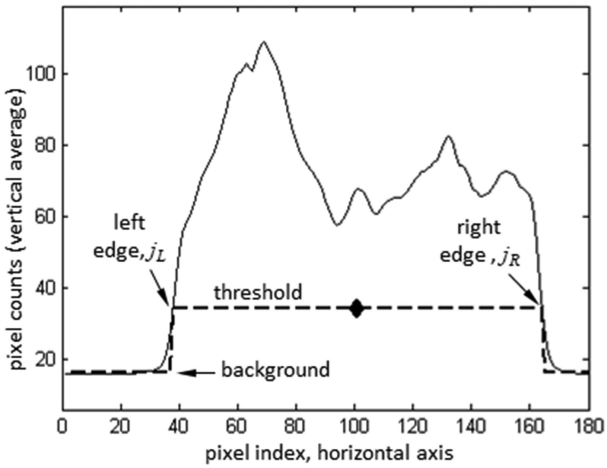

Figure 5. Estimation of the propagated pupil centre in the horizontal axis. The continuous line shows the vertical (column) average of the image. The dashed line defines the values used for estimating the centre (upper segment), while the lower segment of the dashed line is background. The black diamond is the horizontal centre. The same procedure is followed for the estimation of the vertical centre.

pixels is augmented by 20 per cent to determine the number of pixels required to make diffraction leakage negligible (p_2 in Fig. 4). This percentage value has been defined after analysing thousands of frames for different star magnitudes and turbulence conditions.

The estimation of the average background value is now calculated over the range defined by p_2 and p_4, the latter chosen as 95 per cent of the total number of pixels in the image (to reject cold or defective pixels). Finally, the threshold value over which the pixels are considered part of the pupil (p_3 in Fig. 4) is taken as the mean value between p_1 and p_2. This relationship was found empirically and proved to be robust under all conditions encountered so far. For the image in Fig. 3 (side $P = 180$ pixels), the calculated threshold is 34.3 counts, and it is used to calculate the centre of the propagated pupil (diamond in Fig. 5 for the horizontal axis). First, the average of the pixel counts in each column is calculated

$$I_x(j) = \frac{1}{P}\sum_{i=0}^{P-1} I(i, j). \tag{4}$$

By clipping I_x to a binary image (above and below the threshold), the horizontal centre becomes

$$C_x = (j_L + j_R)/2, \tag{5}$$

where j_L and j_R are the leftmost and rightmost points where $I_x(j)$ is larger than the threshold (see Fig. 5).

The same procedure is repeated for C_y (vertical centre). With C_x and C_y calculated for every frame, the image is centred for the subsequent ring extraction described in the next section. Considering the histogram construction shown in Fig. 4, the calculation of the pupil centre takes less than 1.5 ms in current personal computers.

3.2 Construction of angular arrays

Using standard interpolation techniques (see Appendix B) the pupil images at the detector are transformed to a polar grid formed by concentric rings. Fig. 6 shows the case for five rings, all containing the same number of angular elements forming arrays that are Fourier-transformed to obtain the angular power spectra of the scintillation along the sampled circumferences.

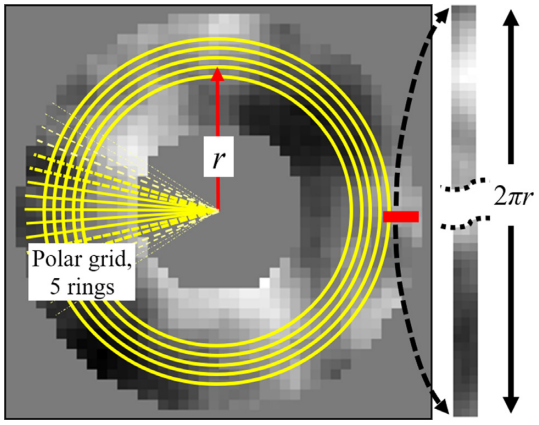

Figure 6. Unravelling the rings.

The benefits of computing angular PSDs on the annulus is two-fold:

(i) It reduces the impact of diffraction rings from the inner and outer pupil edges. This is of great relevance for the NC version to be described later.

(ii) The Fourier-transform is performed for a circular, continuous 1D vector, avoiding leakage due to discontinuities at the edges.

The latter feature is essential in the method, since for a non-circular signal, the variable signal difference between the end and the beginning of the array would contaminate the corresponding spectra in ways impossible to predict and hence correct. By ensuring that the two extremes match, this problem disappears.

3.3 The angular power spectra

We define N_r concentric rings (annulus) within the pupil as shown in Fig. 6. Each ring is divided into an integer number of segments given by $N = 2\pi\,\delta\theta$ with $\delta\theta$ being the angular increment (see Appendix B). The intensity average of N_r segments along the radial direction form the angular array, so for each ring, represented by the sub-index r, its discrete Fourier transform is given by

$$G_{r,m} = \sum_{n=0}^{N-1} I_r(n)\, \mathrm{e}^{-\frac{j2\pi mn}{N}}, 0 \le n \le N, \tag{6}$$

where I_r is the angular array of intensities and m the frequency index. Then, the average PSD for the N_r concentric rings is

$$F_m = \frac{1}{N_r}\sum_{r=0}^{N_r-1} G_{r,m} G^*_{r,m}, \quad {}^*: \text{complex conjugate.} \tag{7}$$

This result is divided by its zero-frequency component to normalize the PSD vector by the total signal in each ring. By repeating this procedure for several images, an estimate of the scintillation PSD is obtained ($\bar{\boldsymbol{F}}$). Since the interpolation described above is generally oversampled to avoid aliasing terms, only a subset of the angular frequencies is used for the profile restoration, as will be explained below.

3.4 Construction of the weighting functions

As mentioned before, this process is performed for the on-sky pupil images and also for the SWFs. The simulated propagation is repeated for 10 uniformly spaced wavelengths between 400 and

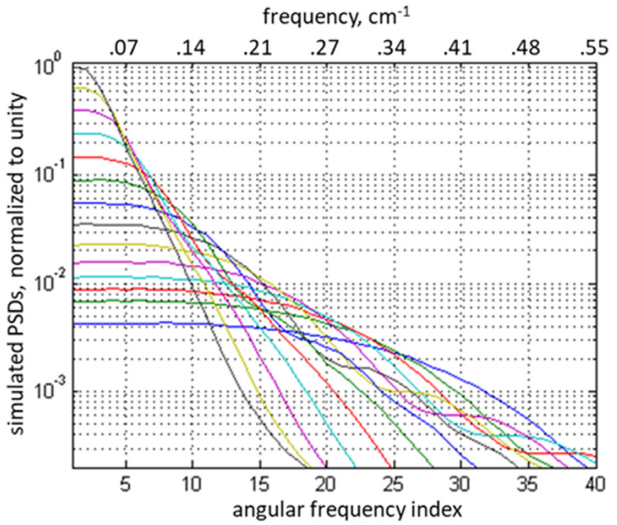

Figure 7. Simulated PSDs of scintillation patterns for each of the 14 layers that form the SWFs. The curves with higher peaks and lower frequencies correspond to the layers located at high altitudes. The top scale shows the average spatial frequency for the N_r rings and the bottom scale correspond to the angular index m. Angular indices higher than 40 are discarded.

700 nm whose intensities are weighted and averaged at the pupil. The atmospheric phase aberrations are realized using the same weak-turbulence strength ($r_0 = 20$ cm). Departure from this weak-turbulence regime can be accounted for by changing the simulation parameters. The simulated scintillation images are later subjected to the same processing as that of the on-sky data and an average of many PSDs is obtained for each layer, forming the matrix **W** for the restoration of the profile.

To construct the SWFs for the free-atmosphere case, we start by defining the distances h_i to the individual layers that will form the basis for the restoration process

$$\boldsymbol{H} = \{.3, .45, .6, .8, 1, 1.4, 2, 3, 4.5, 6, 8.5, 12.5, 18, 25\} \text{ km}. \quad (8)$$

A large set of simulated scintillation images produced for each of the 14 slabs (over 10 000 frames for each layer) are processed to obtain the angular PSDs in Fig. 7. Frequencies higher than the 40th term (equivalent to a spatial frequency of 0.55 cm^{-1}) are thrown away, as they do not contain relevant information due to the polar grid oversampling. This spatial frequency corresponds to Nyquist sampling of 0.9 cm, lower than that of the smallest speckle. This figure also suggests that trying to accommodate more than 14 layers in the restoration basis is debatable, as the contiguous PSDs become increasingly similar, deteriorating the conditioning of the inversion problem.

A striking difference in the maximum strength of the PSDs between lower and higher layers is observed. The higher layers generate low frequency scintillation with PSD amplitudes of around two orders of magnitude stronger than those propagated from the lower layers. This difference imposes a numerical challenge to the restoration algorithm. We alleviate this problem by binning the spectrum at high frequencies, i.e. by progressively increasing the number of binned (averaged) spectral points, the spectrum is reduced from 40 to a 16-element vector that forms the modified frequency vectors $\bar{\boldsymbol{F}}$ and $\hat{\boldsymbol{F}}$ used in the profile-fitting process. We adopt the width of the frequency bins proportional to the actual frequency and use interpolation to account for the non-integer bin limits. We define

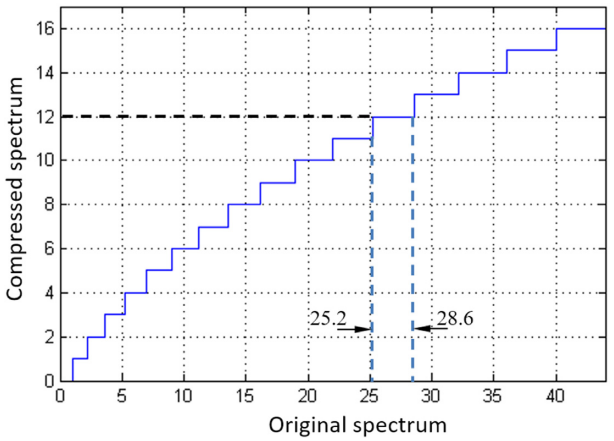

Figure 8. Compression of the spectrum. A progressively larger binning of frequency components at higher frequencies improves the conditioning of the minimum search problem.

the bin centres (frequencies) in our reduced spectrum as:

$$f_i = f_{i-1} + \delta f_i \text{ for } i = \{0, 1, .., 16\} \text{ where } \delta f_i = \delta f_{i-1} + \alpha. \quad (9)$$

The initial values for the recursive equations above are $\delta f_0 = 0.8$ and $f_0 = 0$, and we have found that a value of $\alpha = 0.2$ is a good choice that spans all the frequencies of interest. The reduced (compressed) spectrum is given by

$$F_i^{\text{comp}} = \left(\sum_{k=k_i+1}^{k_f} F_k \right) - \rho_1 F_{k_i} + \rho_2 F_{k_f}, \quad (10)$$

where k_i = floor(f_{i-1}); k_f = floor(f_i); ρ_1 = rem(f_{i-1},1) and ρ_2 = rem(f_i,1).

The compression factor goes from 1.0 for $i = 1$ to 4.0 for $i = 16$ (frequency 0 is not considered). Fig. 8 shows the reduction of the original spectrum. For example, for $i = 12$, $\rho_1 = 0.2$, $\rho_2 = 0.6$, so the bin limits are $k_i = 25.2$ and $k_f = 28.6$, respectively, as indicated by the dashed lines.

3.5 The noise spectrum

There are at least three sources of noise in the pupil image that affect the profile retrieval, namely photon noise, read-out noise, and dark noise. The latter can be neglected, as the short exposure times (1 ms or similar), does not allow the building of a significant number of secondary charges.

The noise contribution to the profile restoration, can be accounted for by defining an additional PSD in matrix **W** which is not an SWF in the strict sense, as it is not constructed out of a turbulence layer. We have tried two ways of estimating the noise PSD; the first uses a phenomenological model for the simulation of the noise frequency response. A second, experimental approach, obtains the noise PSDs from the detector under uniform illumination conditions for photon fluxes similar to those expected from stars used as beacons (magnitudes from $m = -1$ up to $m = 2.5$). Interestingly, no significant differences in the shape of the PSDs were observed between these two methods. This is not surprising, as for the spatial frequencies of interest (given by the inverse of the smallest speckle), the noise PSD resembles that of a white noise in both cases. Possible differences in magnitudes of the PSDs are not relevant in our case since the purpose of the noise-SWF is only to isolate this disturbance from the turbulence restoration.

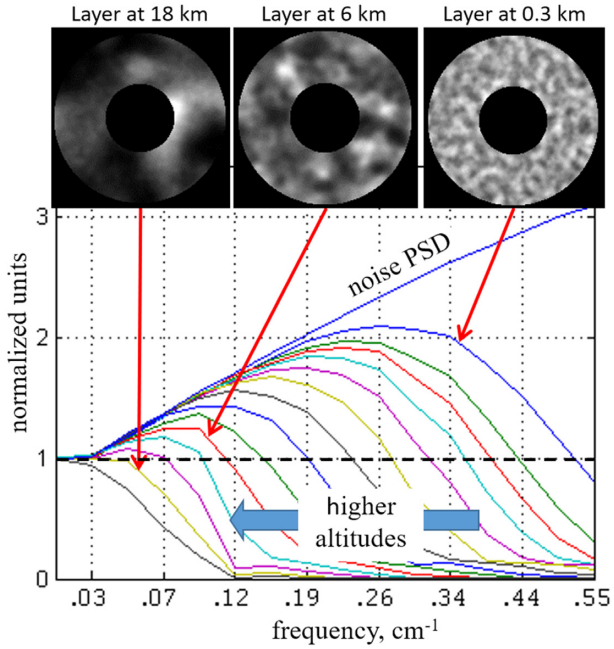

Figure 9. SWFs obtained from angular arrays (unravelled rings). Top: examples of simulated scintillation images at the pupil plane from layers located at three different altitudes. Bottom: normalized SWFs (spectra are show normalized to the first element). The noise PSD has been empirically estimated for the detector in use.

Fig. 9 shows the SWFs that form the basis used for the profile restoration in the free-atmosphere (PC) case. In addition to the 14 spectra contained in the matrix $\mathbf{W}$, the noise PSD calculated as described in equations (9) and (10) is also included. This inclusion allows relaxing the minimum-search problem by absorbing both the noise in the scintillation images and the speckles smaller than those corresponding to the lowest layer (i.e. below 300 m).

In the NC case, this noise function effectively represents the noise in the image as possible leakage from contiguous spectra corresponding to the smallest speckles should be negligible. We define a new matrix $\mathbf{W}'$ that incorporates the noise contribution in the restoration process, $\mathbf{W}' = \begin{bmatrix} \mathbf{W} \\ \boldsymbol{W}_N \end{bmatrix}$, where $\boldsymbol{W}_N$ is a row vector with M elements representing the noise PSD. This augmented matrix $\mathbf{W}'$ implies an augmented coefficient vector $\boldsymbol{x}' = \begin{bmatrix} \boldsymbol{x} \\ x_N \end{bmatrix}$, where x_N is the new coefficient representing the weighting of the noise PSD in the restored profile.

3.6 Optical turbulence profile restoration

As described in Section 2.2, the profile restoration consists of a non-linear minimum search due to the non-negativity constraints imposed on the profile coefficients in $\boldsymbol{x}$. We pose the minimization of χ^2 in equation (3), with $\hat{\boldsymbol{F}} = \boldsymbol{x}'^T \mathbf{W}'$, where $\mathbf{W}'$ is a 15 × 16 matrix and $\boldsymbol{x}'$ a column vector with 15 elements. To find the minimum of χ^2, we use a trust-region-reflective algorithm (Coleman, 1996) as it effectively handles the boundary constraints set by the non-negativity requirements on the x_i coefficients. The search method requires that the number of frequency components in our measured spectrum $\bar{\boldsymbol{F}}$, must be larger or equal to the number of profile coefficients. In our problem posing, this requirement is met as the length of $\boldsymbol{x}'$ is 15 and the number of frequency elements M is 16.

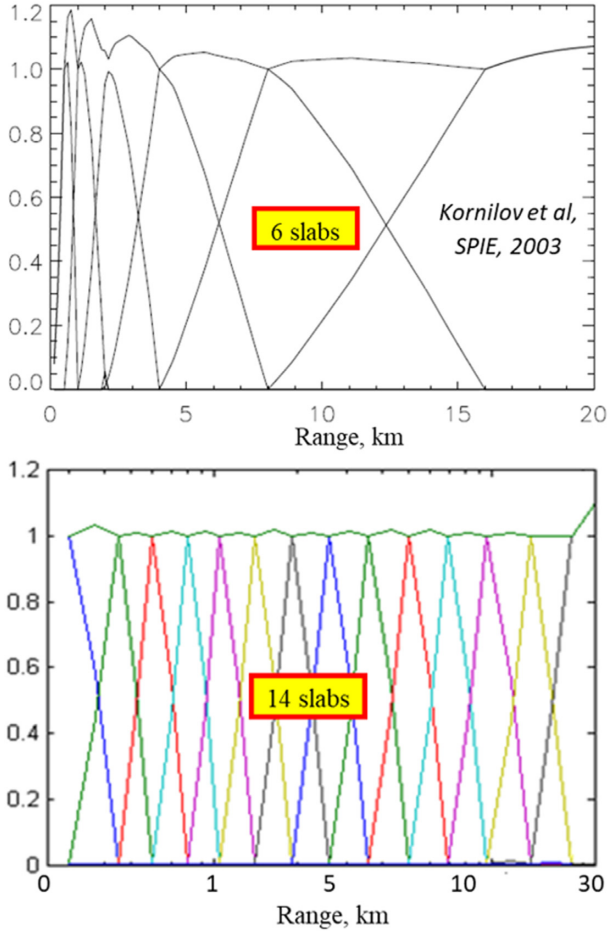

Figure 10. Response of the fixed-layer restoration procedure to a single turbulent layer at variable distances: MASS (top); FASS (bottom).

3.7 Theoretical response functions

One way to evaluate the nominal accuracy of our method is by restoring the profile of one slab at arbitrary distances spanning the full range of interest. These are the so-called response functions shown in Fig. 10 for MASS (top panel) and FASS (bottom panel). An apparent improvement in the number of slabs, i.e. a better resolution, is achieved for FASS and its accuracy measured as the deviation of the sum of all responses with respect to the normalized unity value is also significantly better.

4 ON-SKY RESULTS: THE FASS–SHIMM CAMPAIGN

During 2018 April 27th, 28th, and 29th and May 25th, 26th, and 28th, we tested the technique at the Paranal observatory, collecting simultaneous data from the stereo-SCIDAR, MASS–DIMM, and FASS turbulence profilers. These three instruments were installed in the Paranal platform, pointing to different directions and due to nearby structures in each case, they were also subjected to different ground turbulence.

The stereo-SCIDAR profiler (Osborn et al. 2018) is a high-resolution monitor that also uses scintillation as the principle of probing the atmosphere, and is mounted on one of the 1.8-m AT telescopes with its optics negatively conjugated, providing full profiles (including the ground layer). During this campaign, FASS

was run in the PC mode comparison and analysis are restricted to altitudes higher than 1000 m. In the case of the MASS–DIMM monitor, only data from MASS were used.

During this experiment, FASS was integrated to SHIMM (Shack–Hartmann Image Motion Monitor, Perera et al. 2016; Perera 2018). SHIMM provides estimates of total seeing based on a Shack–Hartmann lenslet array and a commercial CCD camera. Its goal is to offer an alternative to the DIMM technique. Details about the FASS configuration in this dual instrument are given in Appendix C.

An EMCCD camera operated in a 4 × 4 binning mode was used in FASS, reducing the read-out noise but enlarging the effective pixel size to 6.7 mm in the pupil. This sampling is an important parameter since it limits the minimum altitude where the speckles can be reliably detected, as they become comparable to the pupil spatial sampling. Furthermore, the scintillation pattern for the lower layers is extremely weak, lacking sufficient contrast to support the estimation of this type of turbulence.

To avoid a smearing of the speckle pattern due to wind, an exposure time of 1 ms was used, and for a 4 × 4 binning, the camera achieved a maximum frame rate of 153 Hz. For each profile restoration, a data cube of 15 000 frames with a region of interest of 77 × 77 pixels, were processed. The area occupied by the pupil was equivalent to 42 × 42 pixels approximately.

A fast frame rate allows a large set of images to be rapidly acquired and assuming frozen flow, it also allows tracking the speckles as they traverse the telescope aperture, which could potentially be used to do wind profiling.

4.1 A tale of three profilers

Fig. 11 shows seeing and isoplanatic angles for the three pairings of profilers and for altitudes above 1000 m. A very good correlation is observed for the FASS–MASS pair (top panels), whereas for FASS/SCIDAR and MASS/SCIDAR combinations (middle and bottom panels), significant biases are observed for the SCIDAR case. The cause of SCIDAR's discrepancy is currently being investigated.

It must be noticed that the number of correlating points differ among the three combinations as only simultaneous data with time-stamp differences less than 3 min were selected for the comparative analysis. Correlations for the cases with fewer coincidences obviously appears worse.

The good correlation for isoplanatic angle obtained for the FASS/MASS pair (top-right panel in Fig. 11), suggests that in both cases, their turbulence stratification is similar, as θ_0 is highly dependent on h.

Then we analyse the consistency between turbulence profiles measured by the instruments. This comparison is not direct, as the altitude scale is different for the three cases and except for the SCIDAR, the scale is logarithmic. FASS uses the altitude scale defined in equation (8), whereas SCIDAR was run with a constant bin size of 250 m (from 0 to 25 000 m). MASS uses its standard 0.5, 1.0, 2.0, 4.0, 8.0, and 16.0 km distance vector. The ranges in all three profilers are vertical altitudes (corrected by airmass). To enable a comparison of the turbulence stratification, a common altitude vector was used, and the scale was constructed with an increasing separation given by a factor of 1.28 between adjacent altitudes to cover the complete range of interest, namely

$$\boldsymbol{H} = \{1, 1.3, 1.6, 2, 2.6, 3.5, 4.4, 5.6, 7.2, 9.2, 12, 15, 20\}\,\text{km}. \quad (11)$$

This common vertical coordinate vector required an interpolation and resampling for all three profilers. In the case of MASS, only the higher 5 slabs (out of 6) were considered and due to its resolution

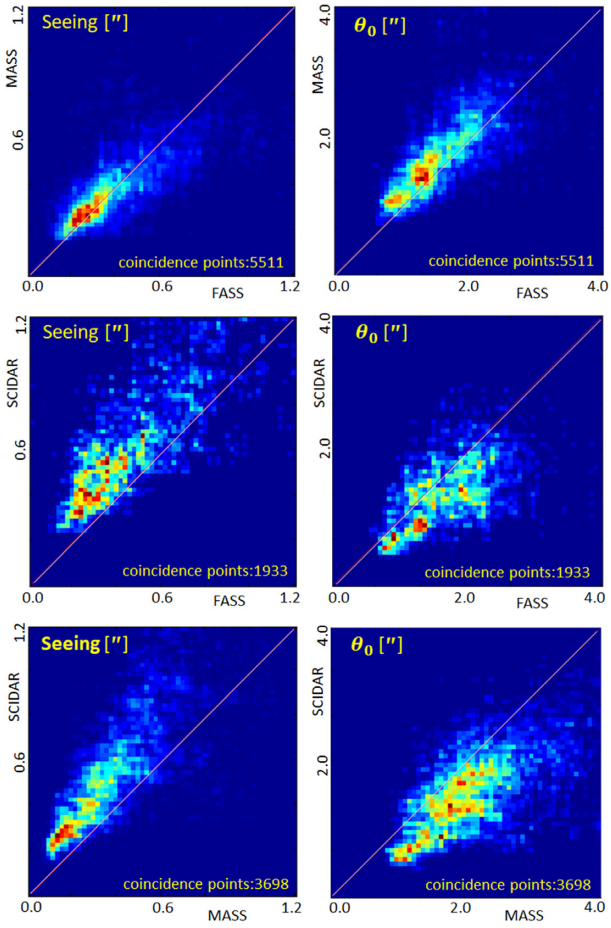

Figure 11. Correlation plots for free-atmosphere seeing and isoplanatic angle. The three possible combinations of profilers with simultaneous data (time-stamp difference less than 3 min), are presented. The best correlation is observed for the FASS–MASS pair. SCIDAR shows significant biases for seeing and θ_0 with respect to FASS and MASS over the ranges of interest.

being lower than the common scale, the J_i value for the 1 km bin was weighed by the fraction of the bin above this altitude.

Despite being in different parts of the Paranal platform, and having different air masses and pointing directions, a remarkable resemblance among instruments were observed. Figs 12 and 13 plot the free-atmosphere profiles J_i for FASS, SCIDAR, and MASS for one night in April and another night in May. In all three sensors, the profiles have been reduced to zenith on the altitude grid.

Consistent results between each pair of instruments are observed. In average, however, the strength for SCIDAR estimations tends to be larger than for the other two, confirming the measurements of the seeing values in Fig. 11. In Appendix D, the comparisons for the other nights are shown (see Figures D1–D5).

One must bear in mind that the profiles can be compared only using simultaneous data and with the same initial and final times. It must be also noticed that the plots are not continuous in time, as voids exist between the beginning and end of each sequence (not shown in the figures).

5 THE NEGATIVE CONJUGATE (NC) FASS

The common weakness of scintillation-based monitors is their blindness to turbulence near the ground. The obvious solution to

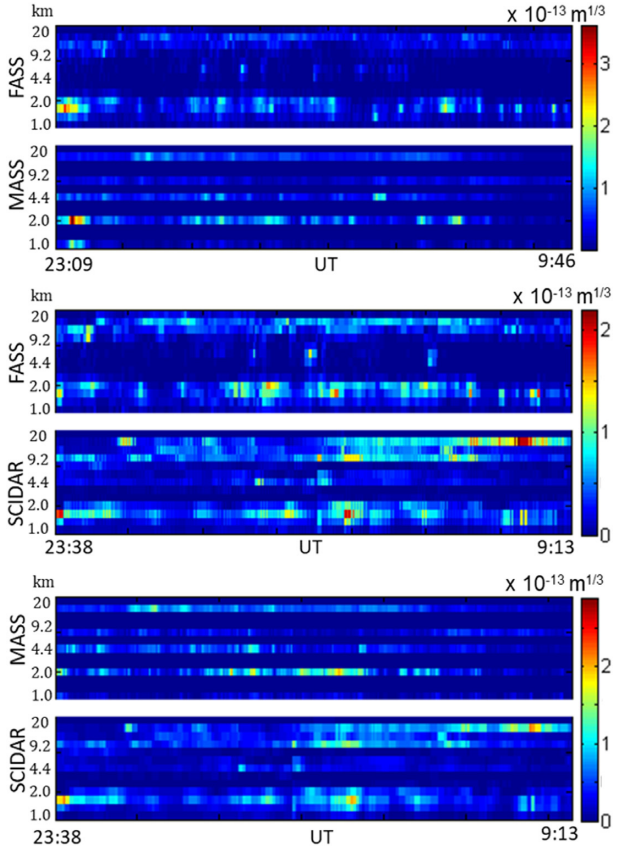

Figure 12. Profiles, 2018 April 27th. Top: FASS–MASS (coincidence points: 1131); middle: FASS–SCIDAR (coincidence points: 347); bottom: MASS–SCIDAR (coincidence points: 629).

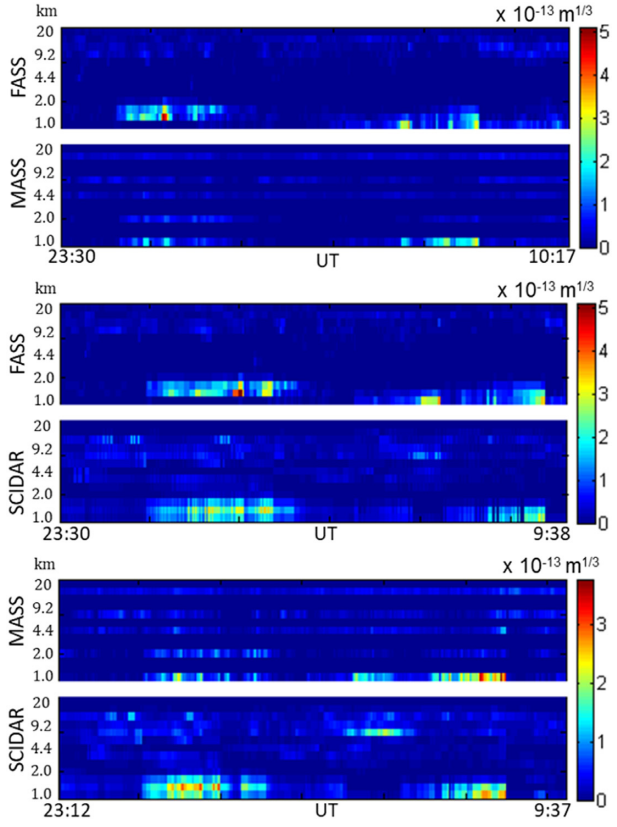

Figure 13. Profiles 2018 May 24th. Top: FASS–MASS (coincidence points: 838); middle: FASS–SCIDAR (coincidence points: 281); bottom: MASS–SCIDAR (coincidence points: 623).

overcome this problem is to allow the propagation of the wavefront below the telescope pupil by means of additional optics (Kluckers et al. 1998; Guesalaga et al. 2016). One of the problems with such approach is the diffraction caused by the telescope aperture on the subsequent negatively conjugated pupil images. Higher sensitivity to vibrations, wind shaking, and optical aberrations (e.g. coma) is also a concern that needs to be addressed.

In this section, we describe the changes made to the original design of FASS to incorporate this extended propagation, while limiting its negative impact on the profile estimation. We started by choosing a larger telescope diameter (12 arcsec), to reduce diffraction distortions caused by the inner and outer edges of the aperture. This larger size also provides longer ring perimeters, delivering better signal-to-noise ratios and accommodating larger speckles generated by high-altitude layers. The telescope F/# number is 8 and the focal length is $f_T = 2.4$ m. We have also changed the detector technology to the new family of scientific CMOS (sCMOS), superior to previous EMCCDs in terms of image quality, framerate, and cost. After testing three commercial camera models with similar specifications and from different manufacturers, we opted for the ZWO's ASI290MM detector, based on cost and lower read-out noise. However, due to its small pixel size (2.9 μm), the read-out noise can still be comparable or even higher than the signal counts per pixel for stars near $m = 2.0$. In the next section, we discuss other detector options with similar read-out noise values but substantially larger pixels; they are being considered in future versions of FASS.

5.1 Pupil apodization

The fact that the scintillation image is circularly sampled in the pupil areas away from the strongest diffraction rings appearing near the pupil edges, substantially mitigates the diffraction problem. Nevertheless, we have studied the benefit of introducing a spatial filter to mitigate the diffraction by smoothing the aperture edges. Inserting an apodizer in the optical path, has the inconvenience that small misalignments of the pupil image with respect to the optical axis, will clip the beam, causing additional distortions. To circumvent this problem, the apodizer can be pasted on the telescope aperture screen; however, this adds a technological challenge and extra costs as no manufacturers offering the large apodizer have been found so far. We have opted for the crude and simple option by accepting some level of diffraction that can still guarantee a good estimation of the turbulence profile. Fig. 14 shows the image of a pupil propagated to −400 m for wavelengths between 400 and 700 nm. The green rings mark the borders of the sampled annulus for the subsequent profile restoration. Ensuring a stable tracking and accurate centring of the pupil image, we can reliably sample the propagated pupil along circumferences that run concentric to the diffraction rings, avoiding the use of apodization screens.

5.2 Optical setup

With no apodization or re-imaging optics, a simple and robust design described by the schematics in Fig. 15 is implemented. Here, we first insert a bandpass filter in the 400–700 nm range, and then introduce a positive lens with focal length f_2 to get a faster system that increases

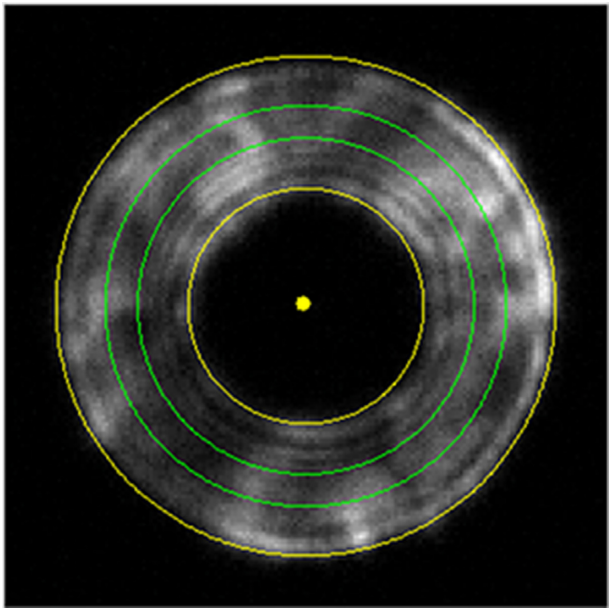

Figure 14. On-sky scintillation image conjugated at −400 m. Green lines define the sampling area for later angular array extraction and processing. Diffraction is noticeable near the edges of the aperture, despite the wide passband filter (400–700 nm).

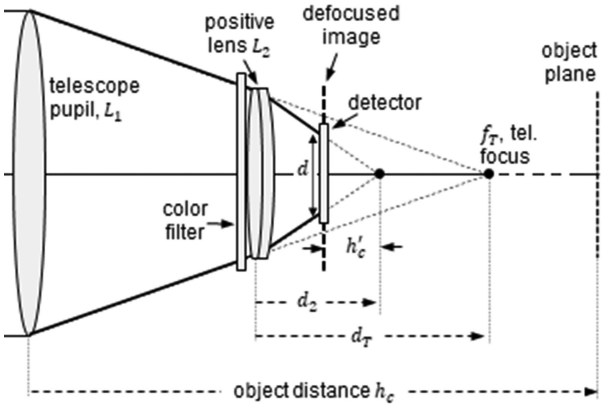

Figure 15. Simplified optics in the current version of FASS. This optical arrangement could reduce possible optical aberrations (e.g. coma) with fewer optical surfaces, i.e. flux losses.

the photon flux per pixel. The detector is defocused from the new star focus by a distance h'_c towards the telescope aperture. Using the geometric optics approximations, we have

$$h'_{\rm c} = \frac{f_{\rm e}^2}{h_{\rm c}}, \tag{12}$$

where $h_{\rm c}$ is the conjugation distance and $f_{\rm e}$ corresponds to the effective focal length resulting from the combinations of the telescope and positive lens, given by $f_{\rm e} = f_{\rm T} f_2/(f_2 + d_{\rm T})$, with $f_{\rm T}$ being the telescope focal length and $d_{\rm T}$ the distance between lens L_2 and the telescope focal point. The pupil size on the detector plane is

$$d = \frac{d_{\rm T} f_2}{f_2 + d_{\rm T}} \frac{D}{f_{\rm T}}. \tag{13}$$

By introducing the positive lens, we can increase the photon flux per pixel from 4 to 10 times. Our goal is to use stars with magnitudes

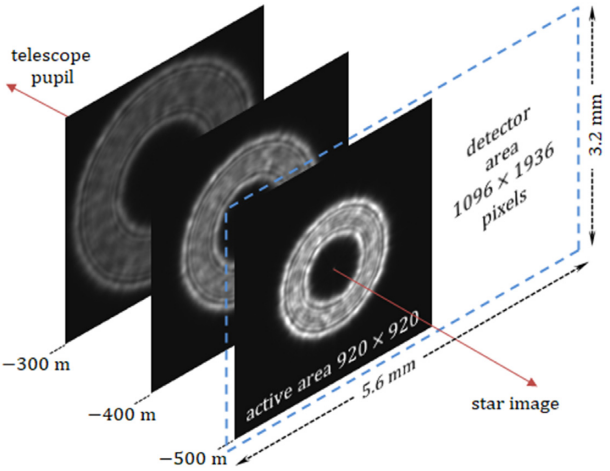

Figure 16. The active area uses 920 × 920 pixels on the left side of the ASI190MM detector. Size and intensity of pupil on detector for three conjugation distances for $f_2 = \infty$.

as faint as $m = 2.5$, so we require a flux larger than the 1 ē read-out noise of the detector in use. Another optical parameter that needs to be defined is the conjugation distance $h_{\rm c}$ and hence $h'_{\rm c}$. The selection of this distance results from a trade-off between several conflicting objectives:

(i) An adequate contrast for scintillation images caused by low-altitude turbulence (weakest contrast case). The longer the extended propagation inside the optics, the better the contrast and counts per pixel

(ii) The image of the propagated pupil must be fully contained in the active area of the detector.

(iii) Limiting the severity of the diffraction rings. The longer the propagation path, the stronger the diffraction rings.

(iv) The size of the smallest speckle must be kept larger than the size of the pixel projected on the pupil.

Fig. 16 shows the image of the propagated pupil at the detector for three possible conjugate distances. To get high photon counts and good scintillation contrast, we need to find a combination of effective focal length $f_{\rm e}$ and conjugation distance $h_{\rm c}$ ($h'_{\rm c}$) that will provide sufficient flux of photons keeping the diffraction pattern at reasonable levels. The −500 m case would seem to be a good choice; however, the diffraction rings are excessively strong, reducing the width of the annulus available for sampling to a narrow circular strip.

After extensive simulations we have found that a good balance between the objectives listed above is $h_{\rm c} = -400$ m. Then, the focal length must be defined to obtain sufficient photon flux per pixel for a star of magnitude $m = 2.5$.

Table 1 lists the optical parameters obtained for three different lenses and for the case with no lens ($f_2 = \infty$). For the latter and for a lens with $f_2 = 50$ mm, no sufficient flux is received in the pixels, reducing the number of available stars that can be used for probing the atmosphere. For a conjugation of $h_{\rm c} = -400$ m, the smallest speckle expected at the detector for $\lambda = 600$ nm is 15.5 mm , i.e. 10 pixels on the detector for $f_2 = 25$ mm. Then, the scintillation pattern is clearly oversampled for any of the lenses in Table 1.

Smearing of the scintillation image due to strong wind is another problem that needs attention. For a conjugation of −400 m, the smallest speckles will be around 1.5 cm for layers near the ground. Ground winds can be effectively handled if the shift occurring during

Table 1. Optical parameters as a function of focal length L_2 and for a negative conjugation $h_c = -400$ m, $d_T = 50$ mm, pixel size $d_{pix} = 2.9$ μm and exposure time of 1 ms.

L_2 focal length, mm	∞	50	30	25
Dist. lens – new focus d_2, mm	50	25	18.8	16.7
Effective focus f_e, m	2.4	1.2	0.9	0.8
Defocus h'_c, mm	14.4	3.6	2.0	1.6
Diameter of virtual pupil d, mm	1.8	0.9	0.7	0.6
Magnification, k	166	333	444	500
Pupil side on detector, pix	620	310	232	206
Smallest speckle in detector, pix	30	15	1	10
Pixel size in pupil, mm	0.5	1.0	1.3	1.5
Counts, $\bar{e}\,\mathrm{pix}^{-1}\,\mathrm{ms}^{-1}$	0.44	1.7	3.1	4.0

the exposure time is smaller than the size of this speckle. For example, during an exposure of 1 ms, a 10 m s^{-1} ground wind will shift the scintillation pattern by 1 cm, and this will increase to 2 cm for a 20 m s^{-1} wind. The obvious solution to mitigate this problem is to use shorter integration times; but unfortunately, read-out noise sets a limit in the minimum required photon count during this period. For the detector currently in use and for an exposure time of 1 ms, this problem can be effectively handled for star magnitudes below $m = 2.0$ and wind speeds no higher than 20 m s^{-1} for the ground layer.

The small pixel size in use is not the optimal choice for fainter stars. New family of detectors with larger pixels (e.g. Canon 35MMFHDXSB 19×19 μm pixel and 2 electron read-out noise) will substantially reduce the smearing problem caused by strong winds. Exposure times shorter than 100 μs will provide sufficient photons for a reliable profile restoration, reducing image shifts to less than 1 mm the loss of speckle contrast to less than 0.5 per cent for winds below 20 m s^{-1}. This will also allow to reach stars of magnitudes up to $m = 2.5$.

Larger pixels could involve aliasing problems when sampling the smaller speckles. For pixel sizes up to 20×20 μm the projected pixel size on the entrance pupil is less than 9 mm or, in terms of spatial frequency, 12 cm^{-1}, which according to Fig. 9 is at least twice the Nyquist frequency required for a correct sampling of the smallest expected speckle.

Other options to increase the photon flux per pixel is the use of optics with deeper conjugation distances (in conjunction with the apodization described earlier). Effective foci shorter than those shown in Table 1 is also an alternative; however, chromatic, and spherical aberrations can become a significant source of distortions.

For turbulence layers at higher altitudes, blurring caused by strong winds becomes less relevant, as speckles grow larger according to the Fresnel ratio $d_s \approx \sqrt{h\lambda}$.

Generally, new sCMOS detectors operate in the rolling shutter mode, which could be another source of spatial image distortions. Sampling a full frame, the extra time taken by this mode is about the exposure period for one line. However, since the region of interest is around a tenth of the total number of lines and the time difference between the top and bottom lines describing a speckle is proportional to its size, for a wind of 20 m s^{-1} and an exposure time of 1 ms, this extra delay generates distortions of less than 1 per cent of the speckle diameter.

5.3 Profile restoration for the NC case

During 2020 February and March, exhaustive testing of the NC mode was carried out at Santa Martina observatory in the outskirts of Santiago, Chile (latitude = 33.4° S; longitude = 70.7° W). This site has poor observation conditions, with seeing values normally larger than 1.0 arcsec. However, it provides excellent facilities for initial testing of this type of instruments.

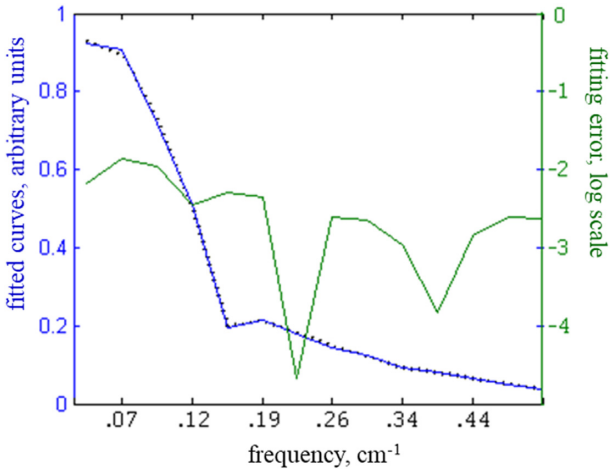

Figure 17. Fitting of the SWFs to the averaged PSDs from on-sky data. Santa Martina observatory, 2020 March 11th.

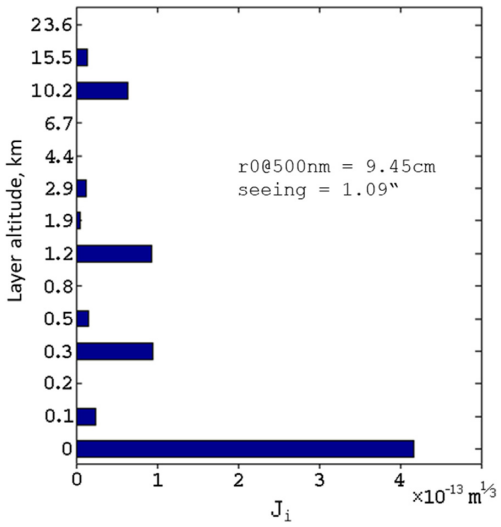

Figure 18. Example of profile restoration; Santa Martina observatory; 2020 March 11th. NOTE: non-linear vertical scale.

Fourteen layers were chosen for the construction of the SWFs (including the ground layer), namely

$$\boldsymbol{H} = \{0, .2, .3, .4, .6, .9, 1.3, 2, 3.1, 4.7, 7.1, 10.8, 16.4, 25\}\ \mathrm{km}. \tag{14}$$

Figs 17 and 18 present an example of profile restoration using Canopus as the beacon star. Fig. 17 shows the SWF fitting (continuous line) to the average measured spectra (dotted line). The green line (right scale) shows the matching error. The fitting delivers the profile shown in Fig. 18.

The NC mode performed extremely well, despite light contamination and poor seeing conditions. Campaigns for exhaustive testing and validation of this mode are being planned in Chile's principal observatories.

6 CONCLUSIONS AND FURTHER WORK

A new technique that measures the vertical distribution of optical turbulence has been described and demonstrated. On-sky experiments validate the method for the free-atmosphere case and preliminary testing show encouraging results for the negative conjugation configuration that leads to a full profile (ground layer included).

Additional work is needed to transform FASS into an observation site monitor. Aspects such as finite exposure and semisaturated scintillation, determining sensitivity limits, streamline data acquisition, real-time processing, and automated operation (pointing and guiding) are still under development.

Estimation of the coherence time based on the method implemented in the MASS–DIMM monitor (Kornilov 2011) is under development. Vertical wind profiling based on temporal cross-correlation of scintillation images (Guesalaga et al. 2016) is also planned for future versions of the instrument.

For the framerates currently in use, only a small fraction of the available light is processed for the profile estimation. We plan to include powerful GPUs in the near future to eventually process all data. However, the benefit of using higher framerates is limited by the strong correlation between consecutive images under typical wind speeds. Simulations and off-line processing of recorded on-sky data show that no significant improvements on the convergence and accuracy of the method is obtained for sampling rates faster than 200 Hz.

ACKNOWLEDGEMENTS

This project is supported by the Chilean Agency for Research and Development (ANID), project Fondecyt 1190186. We also thank A. Tokovinin for valuable advice and comments on the draft version of this paper.

DATA AVAILABILITY

The data underlying this article will be shared on reasonable request to the corresponding author. Data provided by ESO and Durham university will be shared on request to the corresponding author with permission of these institutions.

REFERENCES

Burnashev V. I., 1985, Abastumanskaya Astrofiz. Obs. Bull., 59, 1985(available at ftp://cdsarc.u-strasbg.fr/pub/cats/III/126)
Coleman T. F., Li Y., 1996, SIAM J. Optim., 6, 418
Guesalaga A., Perera S., Osborn J., Sarazin M., Neichel B., Wilson R., 2016, in Marchetti E., Close L. M., Véran J. P., eds, Proc. SPIE Conf. Ser. Vol. 9909, Adaptive Optics Systems V. SPIE, Bellingham, p. 99090H
Kenyon S., Lawrence J. S., Ashley M. C. B., Storey J. W. V., Tokovinin A., Fossat E., 2006, PASP, 118, 924
Kluckers V. A., Wooder N. J., Nicholls T. W., Adcock M. J., Munro I., Dainty J. C., 1998, A&AS, 130, 141
Kornilov V., 2011, A&A, 530, 56
Kornilov V., Tokovinin A., Voziakova O., Zaitsev A., Shatsky N., Potanin S., Sarazin M., 2003, in Wizinowich P. L., Bonaccini D., eds, Proc. SPIE Conf. Ser. Vol. 4839, Adaptive Optical System Technologies II. SPIE, Bellingham, p. 837
Kornilov V., Tokovinin A., Shatsky N., Voziakova O., Potanin S., Safonov B., 2007, MNRAS, 382, 1268
Noll S., Kausch W., Barden M., Jones A. M., Szyszka C., Kimeswenger S., Vinther J., 2012, A&A, 543, A92
Osborn J. et al., 2018, MNRAS, 478, 825
Perera S., 2018, PhD thesis, Durham Univ.
Perera S., Wilson R. W., Osborn J., Butterley T., 2016, in Marchetti E., Close L. M., Véran J.-P., eds, Proc. SPIE Conf. Vol. 9909, Adaptive Optics Systems V. SPIE, Bellingham, p. 99093J
Roddier F., 1981, in Wolf E., ed., Progress in Optics, Vol. 19. North-Holland, Amsterdam, p. 281
Sarazin M., Roddier F., 1990, A&A, 227, 294
Shepherd H. W., Osborn J., Wilson R. W., Butterley T., Avila R., Dhillon V. S., Morris T. J., 2014, MNRAS, 437, 3568
Tatarskii V. I., 1961, Wave Propagation in a Turbulent Medium. Dover Press, New York
Tokovinin A., 2002, PASP, 114, 1156
Tokovinin A., Kornilov V., Shatsky N., Voziakova O., 2003, MNRAS, 343, 891
Vernin J., Roddier F., 1973, J. Opt. Soc. Am., 63, 270
Wilson R. W., Butterley T., Sarazin M., 2009, MNRAS, 399, 2129
Ziad A. et al., 2013, A&A, 559, L6

APPENDIX A: PHOTON COUNTS

The new family of sCMOS detectors appear as excellent candidates for low-light applications such as pupil imaging of faint stars. Here, we describe a methodology to determine the stars that can provide sufficient flux for this type of detectors. We start with the spectral energy distribution (SED) for the star candidates obtained from the available stellar data bases. We use the VzieR III/126 catalogue (Burnashev 1985), compiled for stars brighter than $m = 6.5$ in the 320–817 nm spectral region in steps of $\delta\lambda = 2.5$ nm. The spectrum, $H(\lambda)$, is in units of W cm^{-2}μm, so the corresponding flux of photons can be approximated with

$$H_{\rm ph}(\lambda) = \frac{H(\lambda)}{\epsilon_\lambda}\delta\lambda A \ \ \frac{\rm ph}{\rm s}, \tag{A1}$$

where $\epsilon_\lambda = h_0 c/\lambda$ is the energy of a photon of wavelength λ and A is the collecting aperture area. To calculate the photons effectively converted by the detector, we must include losses due to the atmospheric absorption, the instrument optics and quantum efficiency of the detector. Hence, for an exposure time $T_{\rm exp}$, the number of photons count is

$$H_{\rm ph}(\lambda) = \frac{T_{\rm exp} A\lambda H(\lambda) T_{\rm atm}(\lambda) QE(\lambda) F_{\rm opt}(\lambda)}{h_0 c} \ \ \frac{\rm ph}{\rm s}, \tag{A2}$$

where $T_{\rm atm}(\lambda)$ is the transmission spectrum of the atmosphere; $QE(\lambda)$ is the quantum efficiency of the detector (see Fig. A1); and $F_{\rm opt}(\lambda)$ represents the losses due to the reflective and refractive optics. Our goal is to reach stars brighter than $m = 2.5$ using the ASI290MM camera. For the photon count estimation we have assumed the following settings:

(i) An exposure time of 1 ms.
(ii) The star temperature.
(iii) Optical bandpass filter in the 400–700 nm range.
(iv) Atmospheric transmission at Paranal (Noll et al. 2012).
(v) 10 per cent losses due to optical surfaces.
(vi) Camera with a QE peak of 80 per cent @ 600 nm.
(vii) 2.9 μm pixel size (detector).
(viii) 1.5 mm pixel size (pupil) for a conjugation of −400 m.
(ix) Effective focus $f_e = 0.8$ m.

The spectrum of a star strongly depends on its temperature and since the SWFs are constructed from simulations that take the sun surface temperature as reference (5778° K), stars with temperatures deviations from this reference value will cause estimation errors due entangling of wavelength and altitude represented by the Fresnel law ($d_s \approx \sqrt{h\lambda}$), i.e. hotter stars will produce an overestimation in

the altitude of the layers and the opposite will occur for cooler stars. These altitude biases can be corrected by associating an equivalent temperature to each star (weighted average of wavelengths as exemplified in Fig. A2 for the Sun, Spica, and Gacrux). By using the equivalent wavelength of the sun as reference ($\lambda_{sun} = 545$ nm), deviations in other star temperatures from the latter value ($\delta\lambda = \lambda_{star} - \lambda_{sun}$) can be used to correct the layers altitudes, by multiplying their estimates by $h_s = h/(1 - \delta\lambda/\lambda_{sun})$. Fig. A2 shows the spectra of two extreme stars with different temperatures, Spica (25 300° K) and Gracux (3626° K). Their effective wavelength deviations $\delta\lambda$ with respect to the sun are −56 and +15 nm, causing altitude errors of +10 per cent and −3 per cent, respectively, if no correction is applied.

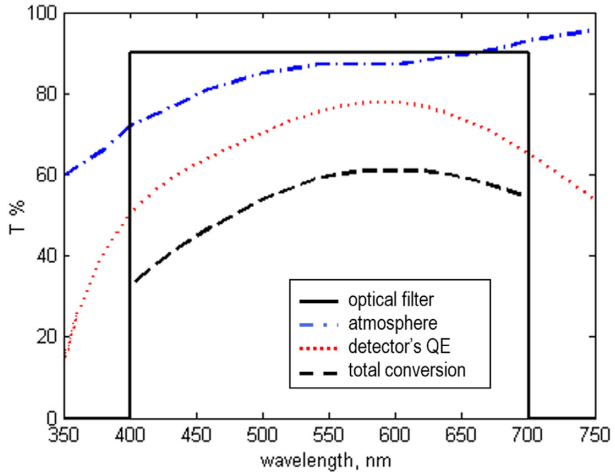

Figure A1. Transmission coefficients: atmospheric absorption for Paranal (Noll et al. 2012) (blue, dot–dashed); ASI190MM detector's QE (red, dotted); optical bandpass (black, continuous); and total conversion efficiency (black, dashed).

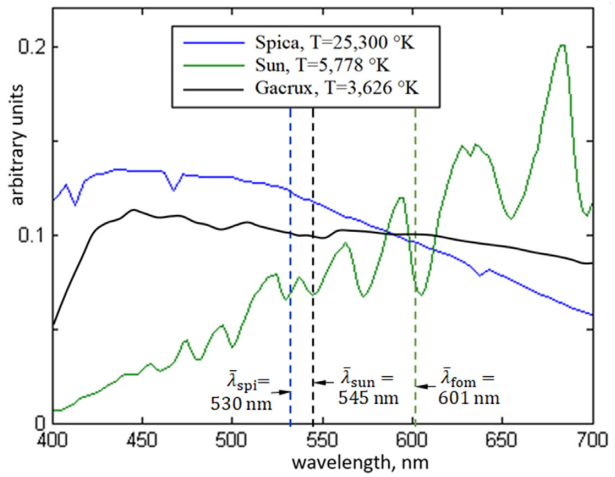

Figure A2. Weightings are corrected for star colour: effective electron counts in the 400–700 nm range for the sun and two stars with different temperatures. Weighted wavelength averages to correct for altitude errors are shown.

Finally, in order to check the performance of the detector for stars close to $m = 2.5$, the number of photons counts per pixel for an exposure time of 1 ms are estimated for two stars with significant temperature differences. The selected stars are η-Cma ($m = 2.45$; $T = 15\,000$ K) and β-Peg ($m = 2.42$; $T = 3689$ K) generate 3.8 $\bar{e}\,pix^{-1}\,ms^{-1}$ and 4.3 $\bar{e}\,pix^{-1}\,ms^{-1}$, respectively, which are well above the read-out noise of the detector.

APPENDIX B: CARTESIAN TO ANGULAR TRANSFORMATION

For the extraction of angular arrays introduced in Section 3.2, the pupil images at the detector are transformed to a polar grid of concentric rings using standard interpolation techniques (see Fig. B1). All rings contain the same number of elements, forming arrays that are unravelled and Fourier-transformed to obtain the power spectra of the scintillation along the sampled circumference

$$I'_{r,\theta} = \alpha\beta I_{x,y} + \alpha(1-\beta)I_{x+1,y} + (1-\alpha)\beta I_{x,y+1} + (1-\alpha)(1-\beta)I_{x+1,y+1}, \quad \text{(B1)}$$

where $\alpha = \mathrm{frac}(r\delta R\cos(\theta\delta\theta))$ and $\beta = \mathrm{frac}(\, r\delta R\, \sin(\theta\delta\theta))$, with $0 \leq \alpha,\beta \leq 1$.

Here, frac is the fractional part of the number and δR and $\delta\theta$ are the radial and angular increments of the polar grid. To avoid aliasing problems due to interpolation, it is required that $\delta R < 1$ and $\delta\theta < 1/R_{max}$, where R_{max} is the radius of the largest ring to be sampled in the image.

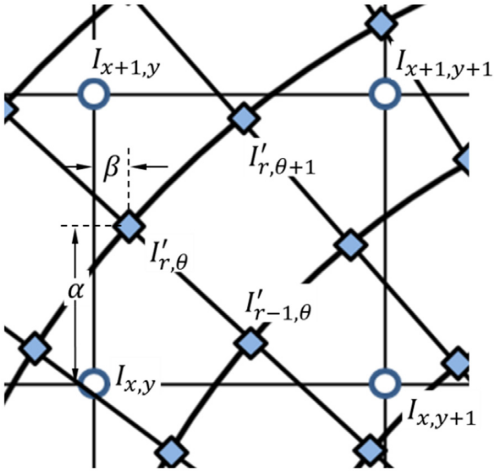

Figure B1. Two-dimensional linear interpolation from Cartesian to polar coordinates. $I_{x,y}$ is the intensity value for pixel $[x, y]$ in Cartesian coordinates whereas $I'_{r,\theta}$ is the interpolated value in polar coordinates $[r, \theta]$. r and θ are whole numbers.

APPENDIX C: CONFIGURATIONS USED FOR PC AND NC EXPERIMENTS

C1 The FASS–SHIMM instrument

This appendix describes the optical set-up and hardware specifications used for the 2018 April and May campaigns, which integrated the FASS and SHIMM instruments (see Fig. C1) in a common telescope, requiring a customized optics to share the incoming light. Fig. C2 shows the FASS–SHIMM optics (top panel) and its optics schematics (bottom panel). Light from the telescope passes through an achromatic lens to produce a parallel beam to the dichroic beamsplitter. The collimated beam is split into two different paths (red and blue arrows in Fig. C2, top) to produce separate images with the same focal ratio for both the SHIMM and FASS optics. This configuration was chosen since scintillation effects are more prominent at shorter wavelengths, which could cause a larger departure from the weak-scintillation regime in the blue. A dichroic at 45° splits the light; wavelengths below 550 nm go to the SHIMM instrument and the reddish ones are used in FASS.

The FASS optics consists of a collimating achromatic lens which images the telescope pupil on to the EMCCD. The SHIMM optics are comprised of an achromatic lens to collimate the light on to the lenslet array. SHIMM was designed to use off-the-shelf components only; however, FASS also required some additional custom mounting components. Table C1 summarizes the main characteristics of the EMCCD camera. It was operated using a 4 by 4 binning to increase the signal-to-noise ratio, resulting in a pupil sampled at 6.7 mm pixel^{-1}.

To reduce smearing of the speckle pattern due to wind, an exposure time of 1 ms was used. Under these conditions, the camera achieved a maximum frame rate of 153 Hz.

C2 sCMOS cameras evaluated for FASS NC case

Table C2 lists the main characteristics of the detectors tested for the

Figure C1. Prototype of the FASS–SHIMM instrument with the optics mounted on a 9 arcsec-*F*/10 Celestron telescope at the VLT site, Paranal, 2018 (Perera 2018).

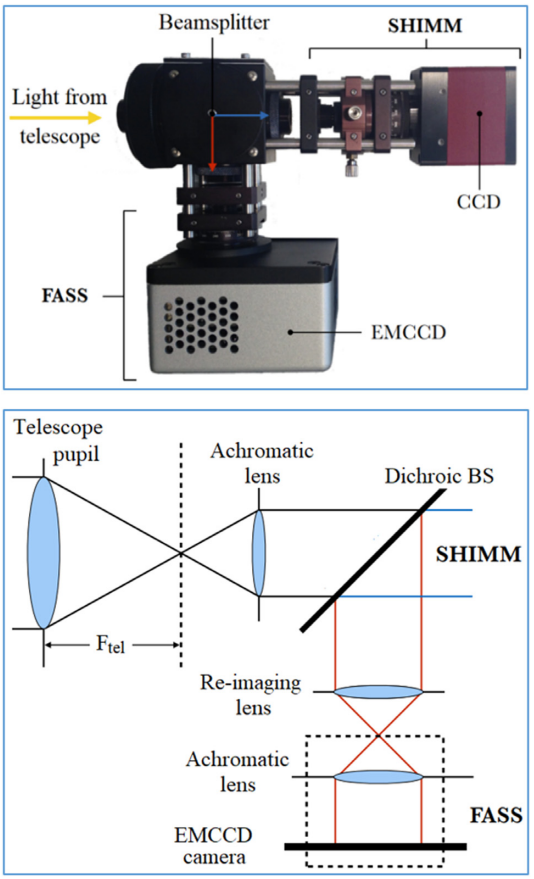

Figure C2. The FASS–SHIMM optics. Top: light from the telescope is split in FASS and SHIMM optical paths, respectively. Bottom: Schematic of the optical configuration of the FASS–SHIMM. Light is collimated before separated by a dichroic that sends longer wavelengths to FASS ($\lambda > 550$ nm) and the shorter ones to SHIMM. In the FASS path, a re-imaging lens is used to generate a negative conjugate of the telescope pupil (Perera 2018).

Table C1. List of the key on-sky specifications of FASS.

Features	FASS detector specifications
Model:	658 × 498 Andor Luca-S EMCCD
Pixel size:	10 μm
Binning:	4 × 4
ROI:	72 × 72
Frame rate:	153 Hz
Exposure time:	1 ms
Image size:	42 pixels
Mapping scale:	6.7 mm pixel^{-1}

Table C2. Specifications of two sCMOS cameras used in the project.

Feature	Edge 4.2bi	ASI290MM
QE peak, per cent	95	80
Pixel size, μm	6.5	2.9
Resolution, pix	2048 × 2048	1936 × 1096
Read-out noise, $\bar{e}$	1.8	1.0
Frame rate (full-frame), Hz	40	20.4
Frame rate (4 × 4 bin), Hz	159	80.2

negative conjugation design and demonstrations. The specifications in both cases satisfied our requirements, so the final selection of the ASI290MM camera was purely based on cost.

APPENDIX D: COMPARISON OF PROFILERS (PARANAL CAMPAIGN, APRIL–MAY, 2018)

The following figures complete the profiles retrieved during the 2018 campaign. Two other nights have been presented in Section 4.

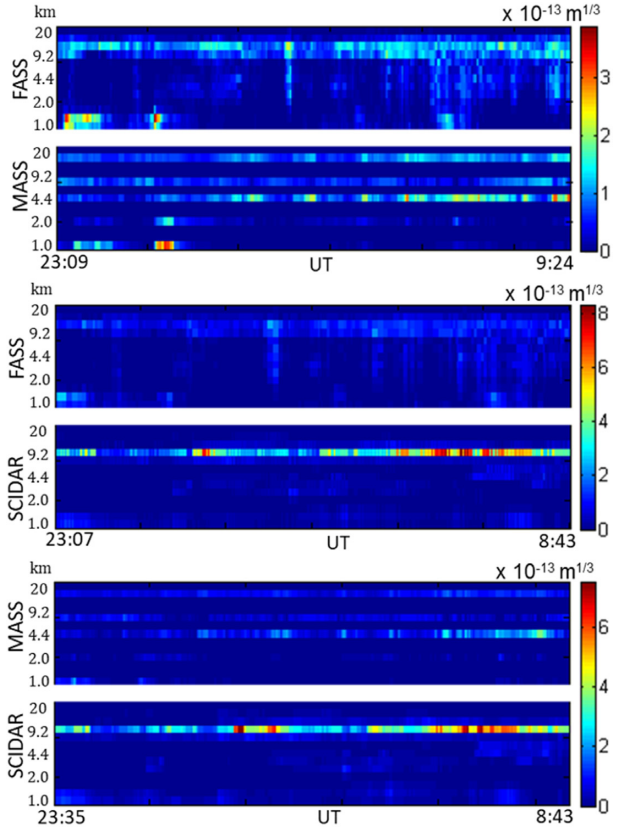

Figure D1. Profiles 2018 April 28th. Top: FASS–MASS (coincidence points: 843); middle: FASS–SCIDAR (coincidence points: 300); bottom: MASS–SCIDAR (coincidence points: 535).

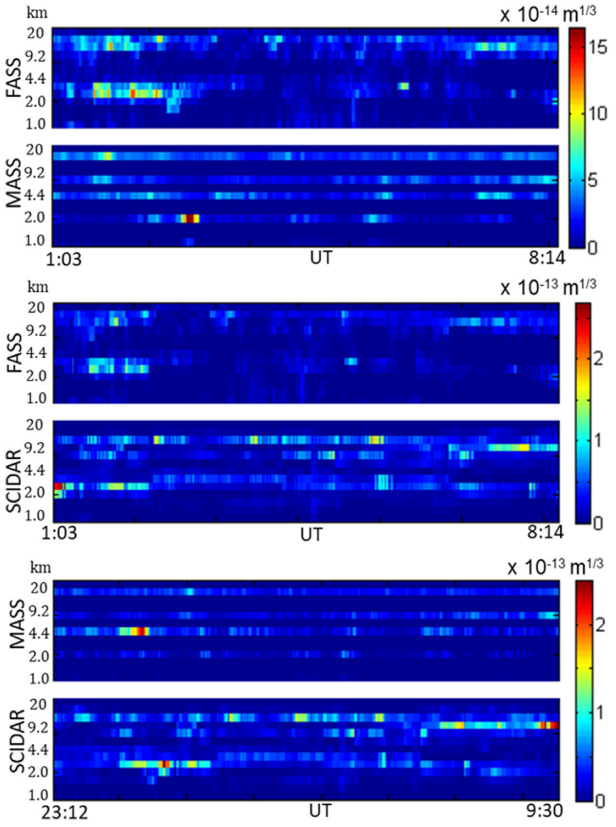

Figure D2. Profiles 2018 April 29th. Top: FASS–MASS (coincidence points: 762); middle: FASS–SCIDAR (coincidence points: 308); bottom: MASS–SCIDAR (coincidence points: 753).

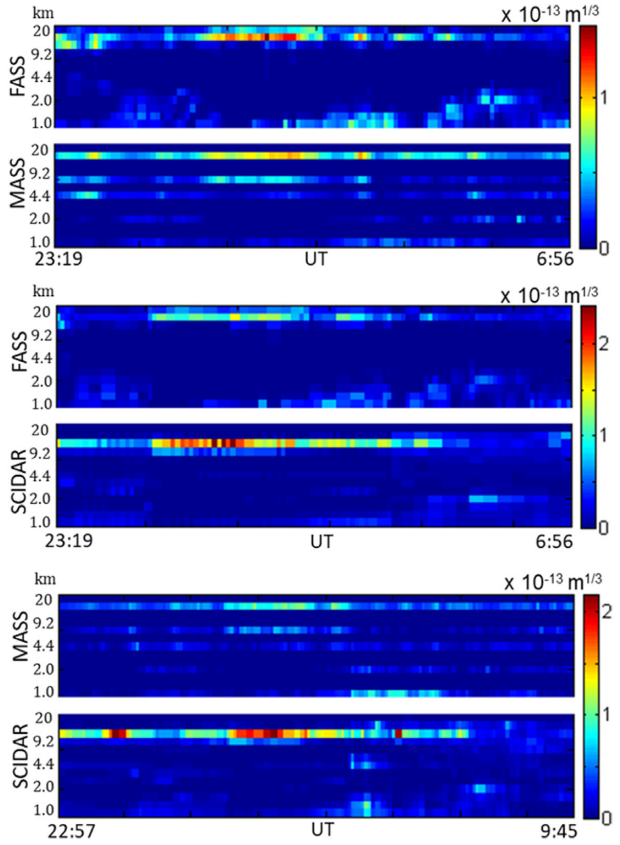

Figure D3. Profiles 2018 May 25th. Top: FASS–MASS (coincidence points: 352); middle: FASS–SCIDAR (coincidence points: 112); bottom: MASS–SCIDAR (coincidence points: 306).

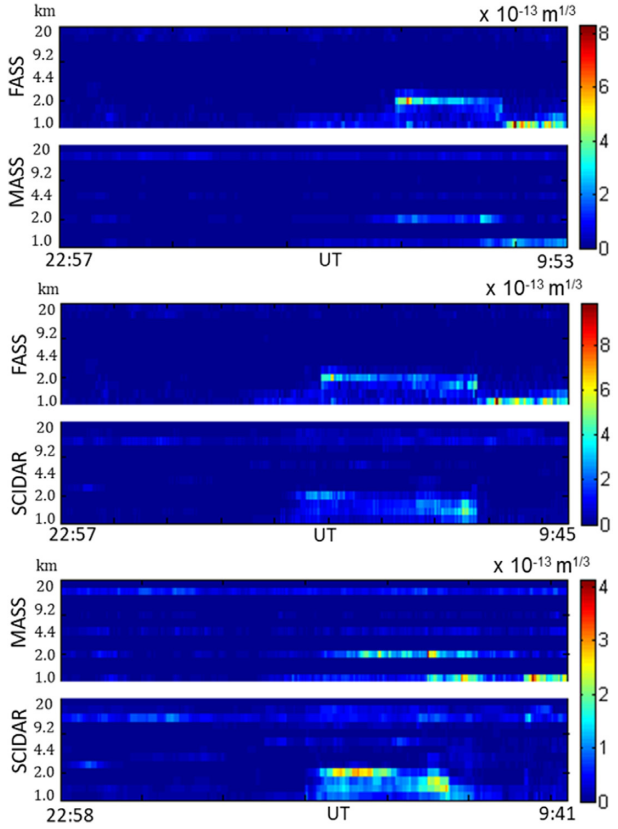

Figure D4. Profiles 2018 May 26th. Top: FASS–MASS (coincidence points: 666); middle: FASS–SCIDAR (coincidence points: 473); bottom: MASS–SCIDAR (coincidence points: 620).

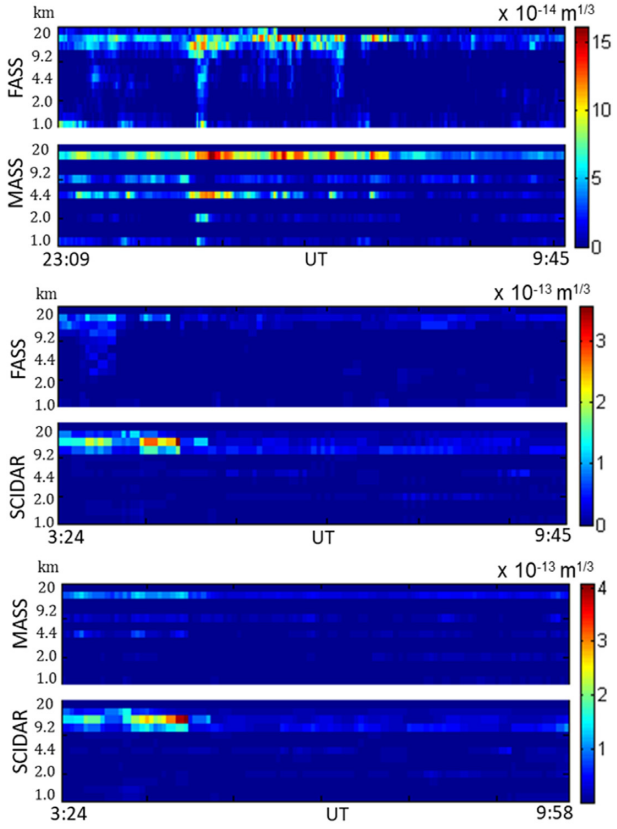

Figure D5. Profiles 2018 May 28th. Top: FASS–MASS (coincidence points: 919); middle: FASS–SCIDAR (coincidence points: 112); bottom: MASS–SCIDAR (coincidence points: 232).

This paper has been typeset from a TEX/LATEX file prepared by the author.